PCCP

Structural evolution of an intermetallic Pd-Zn catalyst selective for propane dehydrogenation

Journal:	*Physical Chemistry Chemical Physics*
Manuscript ID:	CP-ART-01-2015-000222.R2
Article Type:	Paper
Date Submitted by the Author:	26-Feb-2015

Complete List of Authors:	Gallagher, James; Argonne National Laboratory, Chemical Sciences and Engineering Division Childers, David; University of Illinois at Chicago, Department of Chemical Engineering Zhao, Haiyan; Argonne National Laboratory, X-ray Science Division Winans, Randall; Argonne National Laboratory, Meyer, Randall; University of Illinois at Chicago, Department of Chemical Engineering Miller, Jeffery T.; Argonne National Laboratory, Chemical Sciences and Engineering Division

Structural evolution of an intermetallic Pd-Zn catalyst selective for propane dehydrogenation

James R. Gallagher [a], David J. Childers [b], Haiyan Zhao [c], Randall E. Winans [c], Randall J. Meyer [b] and Jeffrey T. Miller [a*]

[a] Chemical Science and Engineering Division, Argonne National Laboratory, 9700 S. Cass Ave., Argonne, IL, 60439 (USA)

[b] Department of Chemical Engineering University of Illinois at Chicago 810 S. Clinton St. , Chicago, IL, 60607 (USA)

[c] X-Ray Science Division, Advanced Photon Source, Argonne National Laboratory, 9700 S. Cass Ave., Argonne, IL, 60439 (USA)

[*]Corresponding author: millerjt@anl.gov

Graphical abstract

Formation of PdZn intermetallic nanoalloys selective for propane dehydrogenation tracked using *in situ* synchrotron XRD.

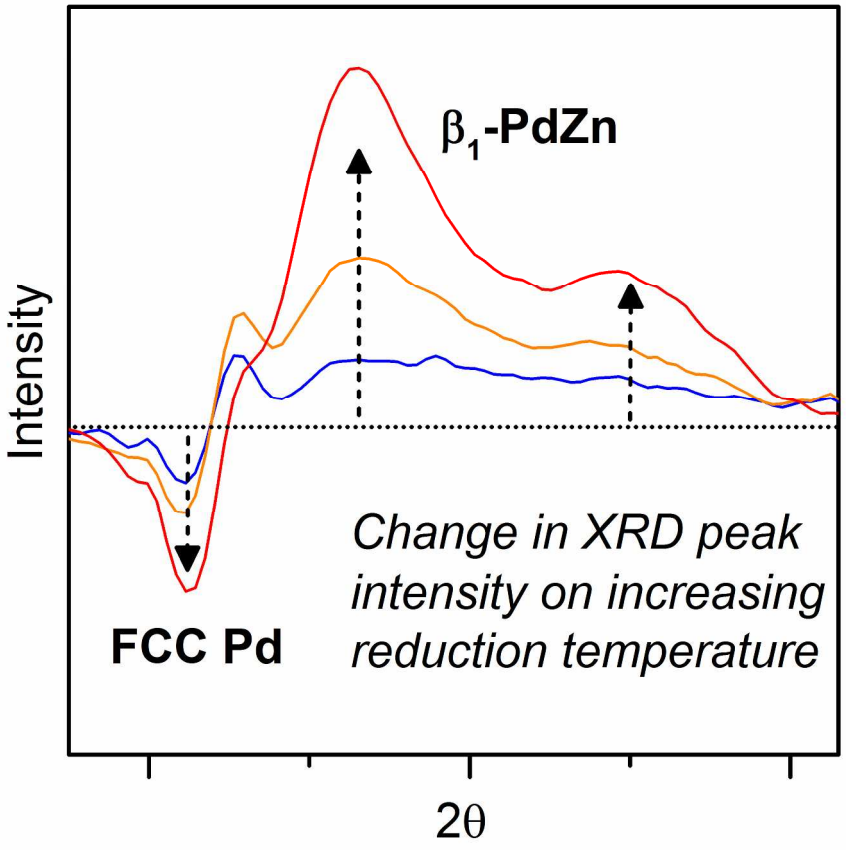

Abstract

We report the structural evolution of Pd-Zn alloys in a 3.6 % Pd – 12 % Zn / Al_2O_3 catalyst which is selective for propane dehydrogenation. High signal-to-noise, *in situ* synchrotron X-ray diffraction (XRD) was used quantitatively, in addition to *in situ* diffuse-reflectance infrared Fourier transform spectroscopy (DRIFTS) and extended X-ray absorption fine structure (EXAFS) to follow the structural changes in the catalyst as a function of reduction temperature. XRD in conjunction with DRIFTS of adsorbed CO indicated that the β_1-PdZn intermetallic alloy structure formed at reduction temperatures as low as 230 °C, likely first at the surface, but did not form extensively throughout the bulk until 500 °C which was supported by *in situ* EXAFS. DRIFTS results suggested there was little change in the surfaces of the nanoparticles above 325 °C. The intermetallic alloy which formed was Pd-rich at all temperatures but became less Pd-rich with increasing reduction temperature as more Zn incorporated into the structure. In addition to the β_1-PdZn alloy, a solid solution phase with face-center cubic structure (α-PdZn) was present in the catalyst, also becoming more Zn-rich with increasing reduction temperature.

Introduction

Alloys are important materials in catalysis science due to the potential for enhancing performance by changing the electronic and geometric properties of catalysts relative to their monometallic counterparts[1, 2]. One sub-class of alloys receiving attention in the literature is that of intermetallics[3-10]. In contrast to random substitutional alloys, intermetallic alloys are characterized by ordered crystal structures, different from those of the constituent metals[11].

The β_1-PdZn alloy possessing the tetragonal $L1_0$ structure is a catalyst which has been widely studied in recent years due to its performance for reactions including the steam reforming of methanol[12-17], dimethyl ether reforming[18] water-gas shift[19] and selective diene hydrogenation[20]. The catalyst is typically prepared by dispersing Pd on ZnO or on a ZnO promoted support, with the Pd-Zn alloy forming *in situ* during reduction or during the reaction. Recently, Childers *et al* demonstrated the use of a Pd-Zn alloy for the selective dehydrogenation of propane to propylene, a reaction for which monometallic Pd catalysts are poorly selective due to their high selectivity towards reactions forming methane and coke[21]. The catalytic performance was attributed to the geometric isolation of the Pd atoms on the surface, turning off the structure sensitive pathways which yield undesired products while promoting the structure insensitive dehydrogenation pathway. As shown in Figure 1, the β_1-PdZn alloy can be described as a tetragonal distortion of the CsCl structure with the Pd atoms in the corners of the cell and the Zn atom at the center. Thus the Pd atoms have only Zn nearest neighbors at a distance of 2.64 Å while the shortest Pd-Pd distance is 2.90 Å, compared to 2.75 Å for face-center cubic (FCC) Pd metal[22].

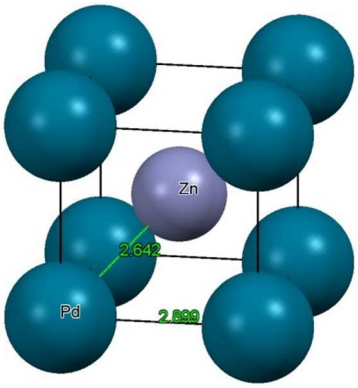

Figure 1. The tetragonal $L1_0$ structure of the β_1-PdZn alloy with the distances (Å) of the shortest Pd-Pd and Pd-Zn bonds shown[22]. Image prepared using the Mercury software[23].

The Pd-Zn phase diagram contains numerous stable phases[24] and therefore after reduction the catalyst may consist of a complex assemblage of reduced and unreduced compounds in addition to the support. X-ray diffraction (XRD) is a useful tool to characterize such complex systems since it is often possible to deconvolute the contributions from each phase. Furthermore, since intermetallic phases are crystallographically distinct from substitutional alloys, XRD can provide information where local structure techniques such as EXAFS may be more ambiguous. XRD has been used extensively to identify the existence of Pd-Zn alloys in the phase assemblage of catalysts[12, 25-28] but little work has been done using high signal-to-noise *in situ* synchrotron XRD to quantitatively investigate the structural evolution of Zn promoted Pd catalysts. While XRD on large nanoparticles facilitates analysis due to sharper diffraction peaks, synchrotron XRD has become increasingly valuable in the *in situ* characterization of catalysts due to the availability of instrument time on high flux beamlines so that high quality data can be collected on complex catalysts containing very small particles and at low concentrations, typical of most research efforts[29-35].

Here we report *in situ* synchrotron XRD, complemented by EXAFS and DRIFTS of adsorbed CO, with the aim of understanding the formation of Pd-Zn alloys in selective propane dehydrogenation catalysts.

Experimental

Catalyst preparation

Two catalysts were synthesized by incipient wetness impregnation; 3.6 % Pd/Al_2O_3 (henceforth Pd/Al_2O_3) and 3.6 % Pd – 12 % Zn/Al_2O_3 (henceforth $PdZn/Al_2O_3$) using spherical alumina nanopowder (NanoDur™, mixture of delta and gamma Al_2O_3, ~ 40 m^2g^{-1}, Alfa-Aesar) as the support. This alumina support has sharp diffraction peaks facilitating the analysis of the XRD patterns. To prepare $PdZn/Al_2O_3$, $Zn(NO_3)_2.6H_2O$ (6.44 g, Sigma-Aldrich) was dissolved in de-ionized water (3.8 ml) and the resulting solution added drop-wise in two stages to Al_2O_3 (10 g) with drying at 125 °C overnight after each impregnation. The resulting solid was calcined at 300 °C in air for 3 h. To the Zn-impregnated solid (8 g) and to pure Al_2O_3 (8 g) was added an aqueous solution of $Pd(NO_3)_2(NH_3)_4$ (8.5 ml for each catalyst, 3.56 % Pd, Sigma-Aldrich) in four stages with drying at 125 °C for at least two hours after each impregnation. After the final drying stage, the resulting solids were calcined at 300 °C in air for 3 h.

Catalyst testing

Propane dehydrogenation selectivity and rate were determined using 66 mg Pd/Al_2O_3 and 503 mg $PdZn/Al_2O_3$ diluted with 0.7-0.8 g silica and loaded into a 0.5" O.D. quartz plug flow reactor. The reactor was purged with Ar for 10 min before each run, and the catalyst was reduced in 4 % H_2/He as the temperature was increased to the reaction temperature of 550 ± 1 °C. Once the reaction temperature stabilized, the reactor was purged with Ar for 10 min before the pre-mixed reactant feed gas consisting of 2.3 % propane/Ar was passed through the reactor. The flow rate of the feed gas was either 20 ml/min ($PdZn/Al_2O_3$) or 30 ml/min (Pd/Al_2O_3) and held constant throughout the duration of the test (300 min) so that the deactivation of each catalyst could be observed.

X-ray absorption spectroscopy

X-ray absorption spectroscopy (XAS) measurements at the Pd K-edge (24350 eV) were performed on the bending magnet beam line of the Materials Research Collaborative Access Team (MRCAT) at the Advanced Photon Source (APS), Argonne National Laboratory. Data was acquired in transmission in step-scan mode using ionization chambers optimized for the maximum current with linear response (~10^{10} photons detected/sec) with 10 % absorption in the incident ion chamber and 70 % absorption in the transmission X-ray detector. A Pd foil spectrum was acquired simultaneously with each sample measurement for energy calibration. Catalyst samples were pressed into a cylindrical sample holder consisting of six wells, forming a self-supporting wafer which was then placed in a quartz tube (1–in. OD, 10–in. length) sealed with Kapton windows by two Ultra-Torr fittings through which gas could be flowed. XAS spectra of $PdZn/Al_2O_3$ were obtained following reduction at 230, 275, 350, 425 and 500 °C at atmospheric pressure in a 4 % H_2/He mixture at 50 ml/min flow rate, while the XAS spectrum of Pd/Al_2O_3 was obtained under the same conditions after reduction at 275 °C. After reduction, the samples were purged with He at 100 ml/min at the reduction temperature and cooled to room temperature in He flow. Trace oxidants in He were removed by passing through a Matheson PUR-Gas Triple Purifier Cartridge. All spectra were obtained at room temperature in He.

The normalized, energy–calibrated absorption spectra were obtained using standard methods and standard data reduction techniques were employed to fit the data using the WINXAS 3.1 software [36]. The EXAFS coordination parameters were obtained by a least-squares fit in *R*-space of the k^2- weighted Fourier transform data from 2.8 to 12.9 $Å^{-1}$, and the fits of the magnitude and imaginary parts were performed between 1.8 and 3.2 Å. Fits were performed by refinement of the coordination number (*CN*), bond distance (*R*), and energy shift (ΔE_0). Experimental phase shift and backscattering amplitude for Pd-Pd scattering was determined using Pd foil (12 Pd-Pd at 2.75 Å). Theoretical phase and amplitude functions for Pd-Zn were calculated with FEFF6 [37] using a two atom calculation, calibrated to Pd foil (using an amplitude reduction factor, $S_0^2 = 0.75$ and a

mean-square disorder, σ^2 = 0.004). The mean-square disorder refined in WinXAS ($\Delta\sigma^2$) reflects the difference in disorder of the nanoparticles relative to the Pd foil. To fit $PdZn/Al_2O_3$, three scattering paths were used; Pd-Pd_{FCC} (unalloyed Pd), Pd-Pd_{PdZn} (alloyed Pd) and Pd-Zn. Reasonable values for *R* and $\Delta\sigma^2$ were determined for Pd-Pd_{PdZn} and Pd-Zn by refinement of the EXAFS after reduction at 500 °C, and the resulting parameters were then fixed for refinements of lower reduction temperature data to allow trends in *CN* to be determined. The same approach was used to determine Pd-Pd_{FCC} by refinement of the EXAFS after reduction at 230 °C, including the Pd-Zn path. ΔE_0 was constrained to be equal for Pd-Pd_{FCC} and Pd-Pd_{PdZn} but was refined independently for Pd-Zn. At 230 °C, 275 °C and 500 °C, only one Pd-Pd scattering path was included in the fit since the Pd-Pd scattering from the majority phase was sufficiently strong to dominate the weaker signal. A Pd-Zn scattering path was included in all fits. Although *CN* can be used to estimate particle size[38] and morphology in monometallic nanoparticles[39], the complex mixture of phases in bimetallic systems makes these analyses unreliable.

X-ray diffraction

In situ X-ray diffraction (XRD) measurements on $PdZn/Al_2O_3$ were performed at the 11-ID-C beamline at the APS, Argonne National Laboratory. Data was acquired in transmission using X-rays at 111 keV (λ = 0.11165 Å) and a PerkinElmer large area detector with typical exposure times of 6 s and a total of 30 scans. Samples were loaded into a 1 mm quartz capillary in a flow reactor [40] which allowed flow of reactant gas through the sample bed during the *in situ* XRD measurements [41]. The reactor was first purged with He for 5 min before a flow of 3.5 % H_2/He at 20 ml/min was introduced and the temperature ramped to 230 °C, holding for 5 min. A measurement was taken at 230 °C before the catalyst was cooled to 40 °C where another measurement was performed. After purging with He to remove palladium hydride species, another measurement was taken at 40 °C in He. Measurements were subsequently obtained in this manner for reduction temperatures of 325, 350, 375, 425, 450 and 500 °C. The bare Al_2O_3 support, in addition to the empty capillary, was treated to the same procedure and reference measurements taken at the same conditions. The 2-D scattering images were integrated to

1-D scattering intensity data using the Fit2D software [42] to yield plots of scattered intensity versus *2θ*. The Le Bail method [43] was used to fit whole XRD patterns between 2.1° and 7.5° 2θ by means of Materials Analysis Using Diffraction (MAUD), a Java-based refinement software [44]. MAUD treats each parameter associated with line broadening separately and thus can be used to deconvolute the contributions from the instrument and from the microstructural features of the sample which broaden the diffraction peaks. The instrumental contribution to the observed peak shape was determined using a standard (LaB_6, NIST SRM 660b) by refinement of the Cagliotti parameters which were then fixed for subsequent refinements of the catalyst samples. In addition to the background polynomial, lattice parameters and isotropic *Delf* particle size[45, 46] were refined for each phase (ZnO, Pd, PdZn) in each sample. For measurements taken after reduction at 230, 325 and 350 °C the lattice parameters and particle size of the β_1-PdZn phase were fixed from the corresponding values from the measurement at 375 °C, refining only the intensities of the diffraction peaks, as the refinement would not reach a stable minimum. Exclusion of the β_1-PdZn phase resulted in a poor fit. Prior to Le Bail refinement, the background scattering from the Al_2O_3 support and capillary were subtracted from the diffraction patterns from the catalysts using the PANalytical High Score Plus software. Where necessary, small regions were excluded from the refinement procedure to minimize artifacts due to background removal.

Diffuse Reflectance Infrared Fourier Transform Spectroscopy

Diffuse Reflectance Infrared Fourier Transform Spectroscopy (DRIFTS) was performed using a Thermo Scientific Nicolet 6700 FTIR spectrometer equipped with a Harrick Scientific Praying Mantis diffuse reflectance *in situ* cell at the Northwestern Clean Catalysis (CleanCat) Core Facility. Samples were ground to a fine powder using a mortar and pestle, and packed into the sample chamber to create a uniform surface. The chamber was purged with Ar before switching to 10 % H_2/N_2 and the temperature raised to 175 °C, holding for 15 min. After reduction of the catalyst, the gas was switched back to Ar and the temperature was reduced to 25 °C. A background scan was recorded, which was averaged over 128 scans (2 minute observation time) with 4 cm^{-1} resolution.

The sample was exposed to 1 % CO/N_2 until equilibrium was reached, at which point the flow was changed back to Ar and a final scan was taken once the intensity of the peak from adsorbed CO was invariant with time. This procedure was repeated for reduction temperatures of 230, 325, 375 and 450 °C for $PdZn/Al_2O_3$ while Pd/Al_2O_3 was reduced at 450 °C according to the same procedure. The ratio of linear to bridge-bound CO reported here do not take into account the differences in extinction coefficients between the adsorption sites and therefore do not represent quantitative coverages, but rather reflect qualitative differences between catalysts[47].

Results

Catalysis

Both the Pd/Al_2O_3 and $PdZn/Al_2O_3$ catalysts were evaluated for dehydrogenation of propane at 550 °C. Catalytic performance is detailed in Table 1 after 15 min (initial), after 50-80 min (middle) where the conversion over both catalysts was 12 % and after 300 min (final). The pure Pd catalyst had an initial rate of 560 mmol g_{Pd}^{-1} h^{-1} but deactivated rapidly; the rate decreasing by over six times in the first 50 min. After 300 min the rate had decreased by almost 16 times, indicating the poor stability of the catalyst. Deactivation was most likely due to coke formation which is produced when propane is converted to methane and ethylene with the olefin further reacting to form high molecular weight species[48, 49]. Coke formation was identified by observation of a blackening of the catalyst and reactor after reaction. The selectivity of the catalyst also varied with time on stream. After 15 min, the majority gas-phase product was methane (98 %) rather than the desired propylene product while after 50 min, the propylene selectivity had increased to 32 %. At the end of the run, where the rate had decreased by almost 16 times (5 % conversion), the propylene selectivity was 77 %. The change in selectivity is likely due to the accumulation of carbon on specific sites highly active for C-C bond scission, leaving behind a modified catalyst able to produce the dehydrogenation product with higher selectivity.

Table 1. Catalytic data for Pd/Al_2O_3 and $PdZn/Al_2O_3$ for the dehydrogenation of propane at 550 °C.

	Pd/Al_2O_3			**$PdZn/Al_2O_3$**		
	Initial (t = 15 min)	Middle (t = 50 min)	Final (t = 300 min)	Initial (t = 15 min)	Middle (t = 80 min)	Final (t = 300 min)
Conversion (%)	77	12	5	17	12	9
Rate (mmol g_{Pd}^{-1} h^{-1})	560	85	35	11	8	6
CH_4 (%)	98	61	21	30	28	22
C_2H_6 (%)	2	3	2	1	0	1
C_2H_4 (%)	0	4	0	6	10	14
C_3H_6 (%)	0	32	77	64	62	64

The catalytic performance of $PdZn/Al_2O_3$ was substantially different from that of the pure Pd/Al_2O_3 catalyst. $PdZn/Al_2O_3$ had an initial rate of 11 mmol g_{Pd}^{-1} h^{-1} which decreased by less than 1.5 times over 80 min. After 300 min the rate had decreased by less than 2 times that of the initial value, demonstrating the higher stability of $PdZn/Al_2O_3$ relative to Pd/Al_2O_3 and suggesting that it is less prone to coking. The behavior in terms of selectivity was also significantly different to Pd/Al_2O_3. Initially, $PdZn/Al_2O_3$ had a propylene selectivity of 64 %, which remained virtually unchanged over the duration of the catalytic test. Comparing the catalysts at the same conversion (12 %) shows that the PdZn catalyst had much higher selectivity to propylene (62 %) relative to the pure Pd catalyst (32 %), despite the increase in propylene selectivity of the latter with time on stream. This demonstrates the selectivity stability in addition to the conversion stability

of the PdZn catalyst relative to Pd/Al_2O_3 with $PdZn/Al_2O_3$ having propylene selectivity close to that at the start.

The propylene selectivity of the $PdZn/Al_2O_3$ catalyst was not as high as the 98 % selectivity reported previously for a $PdZn/SiO_2$ catalyst at similar propane conversion[21], however the present catalyst was not optimized for selectivity but was made for ease of XRD analysis.

EXAFS

To investigate the local structure around the Pd atoms, EXAFS at the Pd K-edge was performed on Pd/Al_2O_3 and $PdZn/Al_2O_3$ at room temperature in He after reduction in H_2. The Fourier transforms of the spectra are shown in Figure 2. The Pd-Pd and Pd-Zn coordination numbers, in addition to the bond lengths, were quantified by fitting the EXAFS data. The fits are shown in Supplementary Figures S1-S6 and the refined parameters are shown in Table 2. The EXAFS of the Pd/Al_2O_3 catalyst was measured after reduction at 275 °C (Figure 2) and confirms the presence of metallic Pd particles as shown by the bond distance of 2.75 Å and the coordination number of 11.2, both of which are close to bulk Pd metal values.

Table 2. Results from *R*-space fitting of the EXAFS data of Pd/Al_2O_3 and $PdZn/Al_2O_3$ measured at room temperature in He after reduction in H_2 at the indicated temperatures. Fitting range; k^2: Δk = 2.8-12.9 $Å^{-1}$; ΔR = 1.8-3.2 Å. *CN* = coordination number; *R* = bond distance; $\Delta\sigma^2$ = mean-square disorder in the distribution of interatomic distances; ΔE_0 = energy offset. The estimated errors are: *CN*, ± 1 and *R*, ± 0.02 Å, within those typical for EXAFS fitting[50]. Pd-Pd_{FCC} = Pd-Pd scattering path from unalloyed Pd; Pd-Pd_{PdZn} = Pd-Pd scattering path from alloyed Pd.

	Reduction temperature (°C)	**Scattering path**	***CN***	***R* (Å)**	$\Delta\sigma^2$ **(Å^2)**	ΔE_0 **(eV)**
Pd/Al_2O_3	275	Pd-Pd_{FCC}	11.2	2.75	0.0005	-0.4
$PdZn/Al_2O_3$	230	Pd-Pd_{FCC}	9.8	2.74	0.0011	-0.4
		Pd-Pd_{PdZn}	N/A			
		Pd-Zn	1.0	2.61	0.0023	-4.8
	275	Pd-Pd_{FCC}	9.1	2.74	0.0011	-0.8
		Pd-Pd_{PdZn}	N/A			
		Pd-Zn	1.5	2.61	0.0023	-3.4
	350	Pd-Pd_{FCC}	6.8	2.74	0.0011	0.0
		Pd-Pd_{PdZn}	2.2	2.90	0.0044	0.0
		Pd-Zn	3.1	2.61	0.0023	-2.6
	425	Pd-Pd_{FCC}	3.4	2.74	0.0011	-0.4
		Pd-Pd_{PdZn}	2.4	2.90	0.0044	-0.4
		Pd-Zn	5.2	2.61	0.0023	-3.3
	500	Pd-Pd_{FCC}	N/A			
		Pd-Pd_{PdZn}	3.7	2.90	0.0044	-1.5
		Pd-Zn	7.9	2.61	0.0023	-4.0

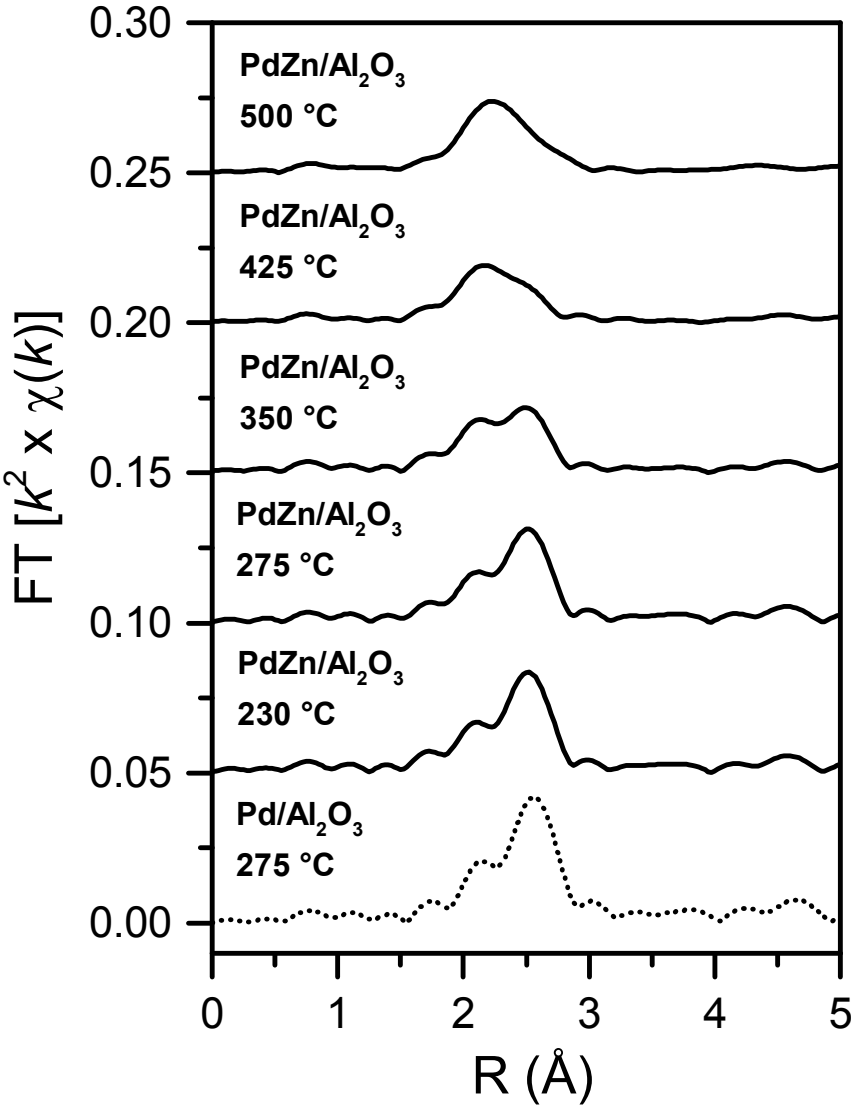

Figure 2. Pd K-edge EXAFS magnitude of the Fourier-transform of Pd/Al_2O_3 and $PdZn/Al_2O_3$ measured at room temperature in He after reduction in H_2 at the indicated temperatures. Plots are offset for clarity. FT range; k^2: Δk = 2.8-12.9 $Å^{-1}$.

$PdZn/Al_2O_3$ was reduced at five different temperatures before cooling in He and measuring the EXAFS spectra at room temperature. The magnitudes of the Fourier-transformed spectra are shown in Figure 2. After reduction at 230 °C there were

predominantly Pd-Pd bonds in the first coordination shell at a distance of 2.74 Å, close to bulk Pd metal. However there was also a non-zero Pd-Zn coordination number (1.0) at a distance of 2.61 Å suggesting that ZnO can be reduced even at very low temperatures in the presence of Pd to form bimetallic nanoparticles. However, the exact structure cannot be decisively determined from local structure techniques such as EXAFS because information beyond the nearest neighbors is limited. Therefore it is not clear whether the alloy is random or ordered or if there are multiple phases present. For instance, this small Pd-Zn contribution could be due to alloy formation occurring at the surface of the particles, leaving behind a Pd-rich core or due to alloys forming in Zn-poor regions of the catalyst.

As the reduction temperature was increased there were large changes in the shape of the EXAFS indicating a transformation from predominantly Pd nearest neighbors at low temperature to a majority of Zn neighbors after reduction at 500 °C. The fits confirm the change in coordination environment with the number of Pd-Pd bonds from the FCC Pd phase (Pd-Pd_{FCC}) in the first coordination shell decreasing from 9.8 to 3.4 as the reduction temperature increased from 230 °C to 425 °C. After reduction at 500 °C, a Pd-Pd_{FCC} contribution could not be refined as the signal was too weak, indicating that there was little remaining unalloyed Pd. As the reduction temperature increased to 500 °C and the Pd-Pd_{FCC} coordination number decreased, there was a simultaneous increase in the Pd-Zn coordination from 1.0 to 7.9, indicating a higher degree of reduction of Zn and increased interaction between Pd and Zn. For reduction temperatures above 350 °C, in addition to the unalloyed Pd scattering path, Pd-Pd_{FCC}, a second Pd-Pd scattering path with longer interatomic distance, from alloyed Pd, Pd-Pd_{PdZn}, was included in the fit. The coordination number of this path increased from 2.2 to 3.7 on increasing the reduction temperature from 350 °C to 500 °C. The final fit after reduction at 500 °C with approximately 8 Pd-Zn nearest neighbors at 2.61 Å and close to 4 Pd-Pd neighbors at a longer distance of 2.90 Å was consistent with formation of a β_1-PdZn ($L1_0$-type) intermetallic structure.

DRIFTS of adsorbed CO

The mode of CO binding on Pd/Al_2O_3 and $PdZn/Al_2O_3$ after reduction at different temperatures was determined by *in situ* DRIFTS at room temperature. The background subtracted spectra are shown in Figure 3. After reduction at 450 °C, the Pd/Al_2O_3 spectrum contained two main peaks due to adsorbed CO in the range 1800-2100 cm^{-1} which correspond to different modes of CO adsorption. Previously; CO has been shown to bind in a bridge fashion, one CO molecule for two surface sites, on terrace and hollow sites, typically giving a vibration in the 1800-1900 cm^{-1} range. Peaks between 1900 and 2000 cm^{-1} have been assigned to bridge-bound CO on corner and edge sites[51, 52]. Linear bound CO, one CO for one surface site, is characterized by two peaks corresponding to corner and edge sites which are typically observed at 2080 and 2050 cm^{-1} respectively[51]. Integrating the peak area between 1800-2000 cm^{-1} and 2000-2200 cm^{-1} yields a linear to bridge bound CO ratio for Pd/Al_2O_3 of 0.44 as shown in Figure 4. These ratios of linear to bridge bound CO do not take into account the differences in extinction coefficients between the adsorption sites and therefore do not represent quantitative coverages, but rather reflect qualitative differences between catalysts.

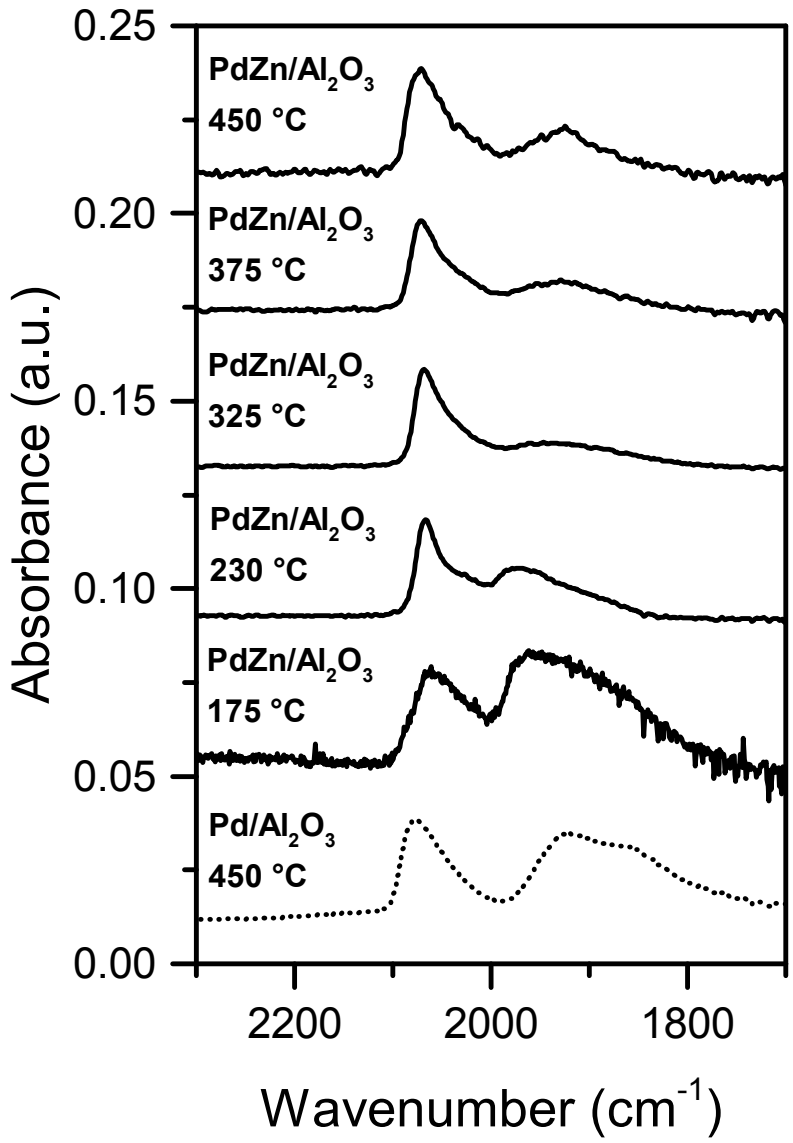

Figure 3. Normalized DRIFTS spectra of adsorbed CO of Pd/Al_2O_3 and $PdZn/Al_2O_3$ measured at room temperature after reduction in H_2 at the indicated temperatures. Plots are offset for clarity.

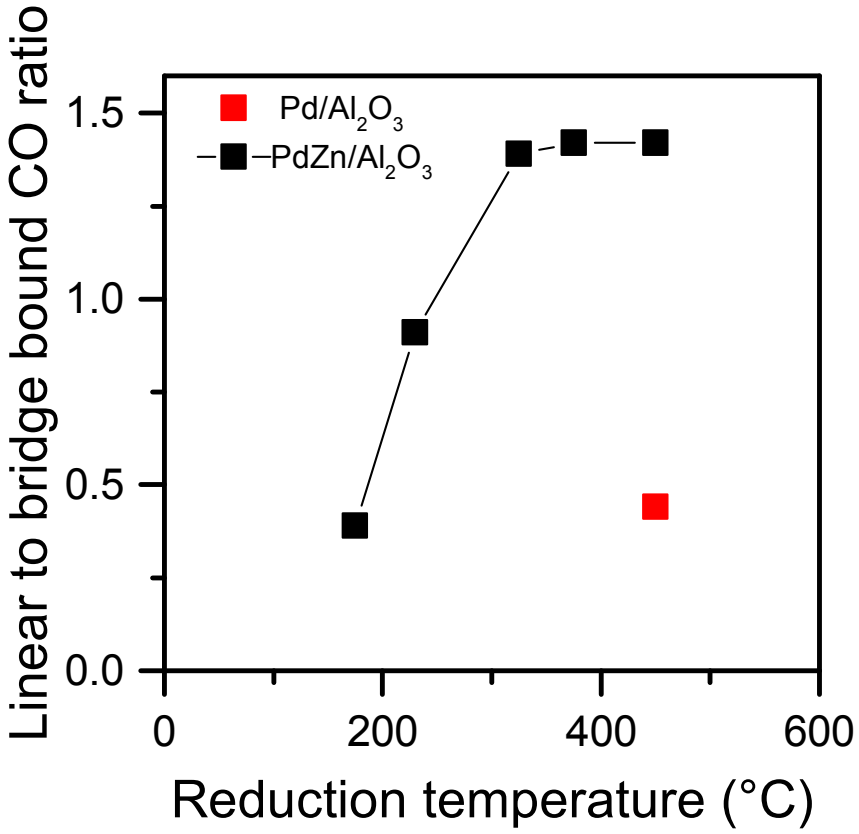

Figure 4. Plot of the ratio of linear to bridge bound CO measured by DRIFTS of Pd/Al_2O_3 and $PdZn/Al_2O_3$ after reduction in H_2 at the indicated temperatures.

The spectra recorded for $PdZn/Al_2O_3$ after reduction at different temperatures are broadly similar to the Pd/Al_2O_3 spectrum, containing two major peaks corresponding to bridge-bound CO at 1800-2000 cm^{-1} and linear-bound CO at 2000-2100 cm^{-1} (Figure 3). However, as shown in Figure 4, the ratio of the integrated peak areas of linear to bridge bound CO changed as a function of reduction temperature. As the reduction temperature was increased the ratio of linear to bridge bound CO increased before reaching a plateau above 325 °C at a ratio of approximately 1.4, which is much higher than the ratio of 0.44 for Pd/Al_2O_3 recorded after reduction at 450 °C. This increase in linear to bridge bound CO indicates that the surface structures that formed in increasingly high concentrations as the catalyst was reduced at higher temperature decreased the ability of CO to bind in a bridging fashion. Since Zn cannot chemisorb CO efficiently, this is attributed to the

insertion of Zn atoms into the surface structures, thus increasing the distance between Pd surface sites. Changes in the linear to bridge bound CO ratio due to reduction temperature have been observed previously[9, 53]. At reduction temperatures greater than approximately 325 °C there was little change in the DRIFTS spectra which indicates that the surfaces which adsorb CO do not considerably evolve on reduction at temperatures up to 450 °C. This suggests that any surface capable of incorporating Zn into its structure can do so at temperatures lower than 325 °C.

XRD

In situ synchrotron XRD was performed on $PdZn/Al_2O_3$ after reduction at different temperatures to understand the phase assemblage at various points in the formation of the alloy. To isolate the diffraction features arising from the phases of interest (ZnO, Pd and Pd-Zn alloys), the diffraction patterns from the bare Al_2O_3 support, heated to the same temperatures, were subtracted from the patterns of the $PdZn/Al_2O_3$ catalysts and the resulting data is shown in Figure 5. This approach has previously allowed extraction of the diffraction features from 1-2 nm Pt nanoparticles dispersed on the same Al_2O_3 support[34]. The fitted parameters resulting from Le Bail analysis of the Al_2O_3 subtracted diffraction patterns taken in He at 40 °C are shown in Table 3 and the plots showing the refined calculated fits are shown in Supplementary Figures S7-S13. Measurements performed on $PdZn/Al_2O_3$ at 40 °C in H_2 (not shown) showed the presence of Pd hydride phases after reduction at all temperatures, which manifested as shifts in the lattice parameters of the Pd phase. Data collected at the reduction temperature in H_2, where the temperature was too high for bulk Pd hydride to form, were consistent with those taken at 40 °C in He. Lattice parameter shifts to longer distance, consistent with increased thermal vibration were observed for all phases at high temperature making analysis of changes in lattice parameter due to changes in the structures difficult. Therefore in the following discussion all comparisons of changes in structure are made by reference to the data collected at 40 °C in He.

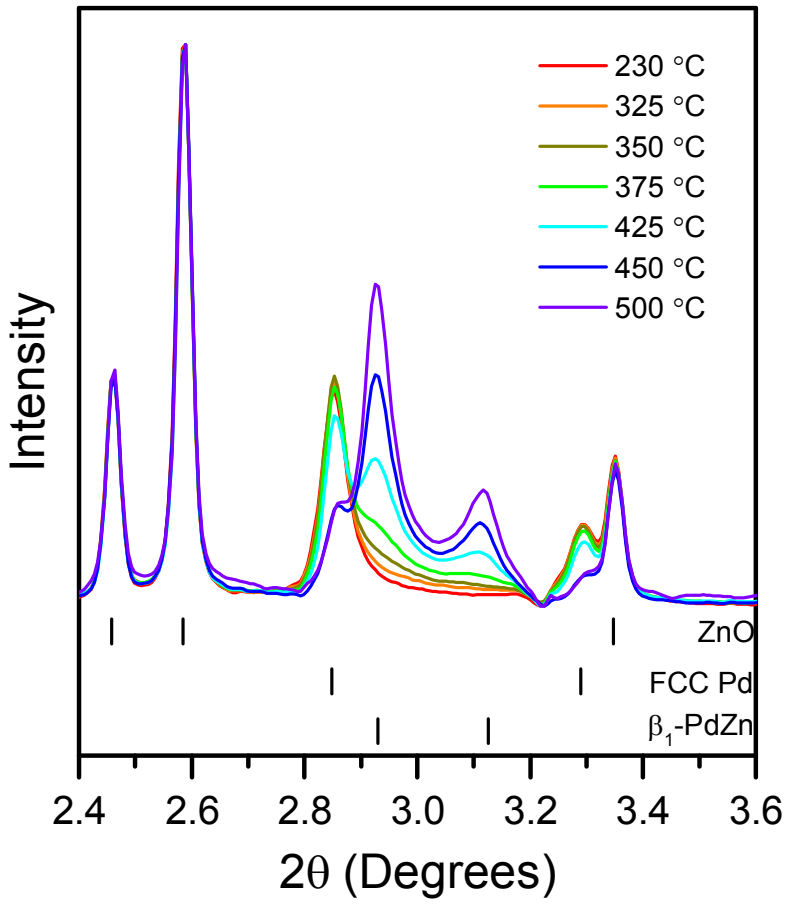

Figure 5. *In situ* synchrotron XRD patterns of support-subtracted $PdZn/Al_2O_3$ measured in He at 40 °C after reduction in H_2 at the indicated temperatures. Tick marks at the bottom of the figure indicate the reference peak positions (ZnO[54], Pd[54] and β_1-PdZn[22]). Plots over a wider angular range are shown in Supplementary Figures S7-S13.

All diffraction patterns clearly contained peaks from ZnO and Pd metal while the intensity of peaks from the β_1-PdZn intermetallic increased as the reduction temperature increased, becoming the dominant Pd containing phase after reduction at 500 °C. No formation of $ZnAl_2O_4$ or pure hexagonal close packed Zn metal could be detected. ZnO (wurtzite) was refined in the hexagonal *P63mc* space group, Pd refined in cubic *Fm-3m* and β_1-PdZn as the tetragonal phase in *P4/mmm*. Although visual inspection of the support-subtracted diffraction patterns in isolation showed little evidence of the β_1-PdZn phase at temperatures below 375 °C, comparing all the diffraction patterns together allowed identification of peak intensity in the 2θ region of 2.9-3.2°, which corresponds to

the β_1-PdZn phase. These features became even clearer when the diffraction pattern measured after reduction at 230 °C was subtracted from those at 325, 350 and 375 °C (Figure 6). Thus even at these relatively low reduction temperatures, the intermetallic β_1-PdZn phase started to form. Additionally, it should be emphasized that while the amount of FCC Pd decreased with increasing temperature, it did not disappear completely at any reduction temperature.

Table 3. Results from Le Bail refinement of $PdZn/Al_2O_3$ *in situ* XRD data taken at 40 °C in He after reduction in H_2 at the given temperature. Quoted errors are estimates based on the standard uncertainty in the powder diffraction pattern intensities and should be considered as lower bounds. The statistical errors on the particle size measurements are smaller than the precision to which they are quoted.* Denotes that these values were fixed from refinement of $PdZn/Al_2O_3$ reduced at 375 °C.

Reduction temperature (°C)	**Lattice parameters (Å)**					**Particle size (nm)**		
	Pd *(Fm-3m)*	PdZn *(P4/mmm)*		ZnO *(P63mc)*		Pd	β_1-PdZn	ZnO
	a	*a*	*c*	*a*	*c*			
230	3.8850(5)	2.9239*	3.2886*	3.2486(1)	5.2039(4)	11	3*	43
325	3.8843(4)	2.9239*	3.2886*	3.2484(1)	5.2035(4)	11	3*	41
350	3.8848(3)	2.9239*	3.2886*	3.2484(1)	5.2033(3)	14	3*	42
375	3.8835(3)	2.9239(12)	3.2886(25)	3.2482(1)	5.2027(3)	16	3	42
425	3.8828(4)	2.9201(8)	3.2853(19)	3.2479(1)	5.2021(3)	19	5	43
450	3.8805(9)	2.9134(7)	3.2967(14)	3.2474(2)	5.2011(4)	20	6	40
500	3.8785(9)	2.9085(6)	3.3059(13)	3.2477(2)	5.2016(5)	20	8	39

β_1-PdZn has a large composition range over which the structure is stable (44-63 at% Pd)[24] and therefore it must possess defects such as anti-site disorder (for example; Pd in Zn sites) or vacancies to accommodate stoichiometries which deviate from equimolar composition[22]. Although it was not possible to determine the fraction of Pd and Zn atoms in the β_1-PdZn from the peak intensities, the lattice parameters of the phase provide some insight into the composition of the intermetallic. For all reduction temperatures, the lattice parameter *a* was larger than that expected from equimolar bulk β_1-PdZn (2.8992 Å) while *c* was smaller than the expected value of 3.3331 Å [22]. However as the reduction temperature increased, the lattice parameters approached the equimolar bulk values. Comparing the extracted lattice parameters to studies where materials were synthesized with varying Pd:Zn ratios[55] indicates that the PdZn structures which formed were Pd-rich, in the 56-60 at% range. The particle size or more precisely, the size of the coherently diffracting β_1-PdZn domains, increased with temperature from around 3 to 8 nm, as the phase fraction increased.

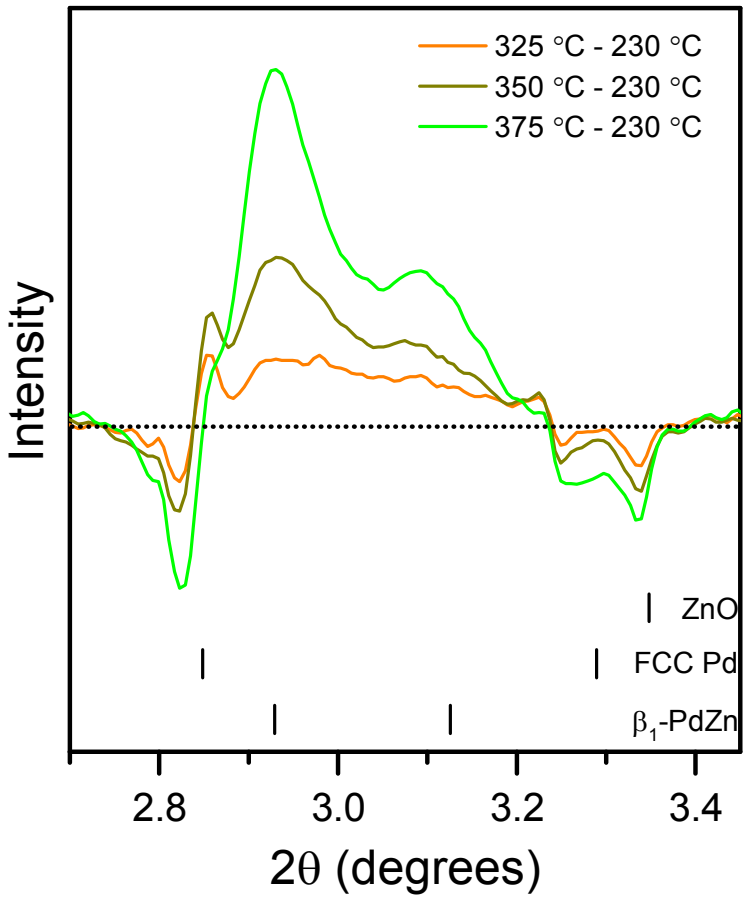

Figure 6. *In situ* synchrotron XRD patterns of support-subtracted $PdZn/Al_2O_3$ measured in He at 40 °C after reduction in H_2 at 325 °C, 350 °C and 375 °C all after subtraction of the equivalent XRD pattern measured after reduction at 230 °C. Intensity above the dotted line indicates an increase in the intensity of the diffraction peak relative to the measurement taken after reduction at 230 °C and *vice versa* for negative intensity. Tick marks at the bottom of the figure indicate the reference peak positions.

The FCC Pd phase also had some differences to that expected for pure bulk Pd (a = 3.8898 Å)[54]. The lattice parameter after reduction at the lowest temperature of 230 °C was 3.8850(5) Å, which, considering the error on the measurement, is slightly smaller than the reference, suggesting formation of the random substitutional alloy α-PdZn which is stable in the Pd-rich region of the Pd-Zn phase diagram[24]. Due to the smaller atomic size of Zn relative to Pd, incorporation of Zn into the FCC Pd structure causes a contraction of the lattice. The lattice parameter decreased with increasing reduction

temperature to a value of a = 3.8785(9) Å, tending towards the value of a = 3.866 Å reported by Halevi *et al*[56] for a α-PdZn alloy containing 11.1 at% Zn, supporting the assertion that there was some Zn incorporation into the FCC Pd structure. Even after reduction at 500 °C, there was still a small amount of Pd that had not converted into the β_1-PdZn phase which could be present either as a core, surrounded by β_1-PdZn or as separate particles. Assuming Vegard's law and using the lattice parameter reported by Halevi for 11.1 % α-PdZn and the value for pure Pd suggests that the amount of Zn in the solid solution increased from approximately 2 at% to 5 at% as the reduction temperature was increased from 230 °C to 500 °C.

In addition to the changes in the metallic components of the catalyst, there was also a small modification to the ZnO phase with increasing reduction temperature. The ZnO unit cell volume slightly decreased from 54.92 $Å^3$ to 54.86 $Å^3$ with increasing reduction temperature which could be due to a partial reduction of the ZnO phase. This would cause the structure to become slightly sub-stoichiometric in oxygen content leading to vacancies, causing the unit cell to shrink.

Discussion

All three characterization techniques used in this study suggest that Pd-Zn alloys can form at temperatures at least as low as 230 °C and XRD implies that there was a mixture of ordered, intermetallic β_1-PdZn phase in addition to a Pd-rich random substitutional alloy, α-PdZn, similar to FCC Pd. The amount of β_1-PdZn was very small after reduction at 230 °C and the diffraction peaks were too weak for the phase to be refined, yet removal from the refinement resulted in a poor fit. Reduction at 325 °C increased the fraction of β_1-PdZn, as shown in Figure 6 by the small increase in intensity in the 2θ region of 2.9-3.2°. At this temperature, as with the measurements at 230 °C and 350 °C, the diffraction peaks were too weak to be satisfactorily refined, but qualitatively, it is clear that the phase was present. Low temperature alloy formation has been reported previously[12, 26, 57] and is postulated to occur by initial reduction of PdO to form Pd nanoparticles, capable of activating H_2 which can then spillover to reduce ZnO [58].

While the IR spectra indicated that there were no further changes in the surface structures above approximately 325 °C, both EXAFS and XRD indicated a continual increase in the fraction of metallic Zn atoms up to 500 °C. This was accompanied by a simultaneous decrease in the amount of Pd-rich random substitutional alloy, α-PdZn. This data provides strong evidence for the 'inward growth' mechanism proposed previously where alloy formation starts at the exterior and moves towards the Pd-rich core[28, 59]. Such growth of β_1-PdZn has been suggested to occur topotactically on the surface of Pd nanoparticles[57].

The lattice parameters of the β_1-PdZn phase suggest that the intermetallic phase was Pd-rich at all reduction temperatures meaning that there must be some defects present in the structure. Previously, calculations have shown that anti-site disorder is the most likely mechanism by which the Pd-rich composition can be accommodated[60]. This implies that even though the β_1-PdZn phase formed, the Pd atoms were not as isolated from each other as they would be, were a perfect 1:1 Pd:Zn ratio realized, since statistically there will be some proportion of Pd-Pd neighbors at a closer distance than in the stoichiometric composition. This has implications for catalysis since the unfavorable reaction of propane to form CH_4 most likely occurs on Pd ensemble sites. Although the β_1-PdZn phase was always Pd-rich, as the reduction temperature increased the lattice parameters did tend towards those of equimolar β_1-PdZn. Furthermore, the absence of any Zn-rich alloys in the XRD patterns is consistent with the assertion by Iwasa that β_1-PdZn selectively forms in Pd/ZnO catalysts because spillover of H from Pd to ZnO is quenched once PdZn is fully formed[13]. The plateau in the linear to bridge bound CO ratio suggests that higher reduction temperatures would do little to increase the number of isolated sites and therefore for the catalyst studied here, the stoichiometry of the β_1-PdZn phase may be limited by the catalyst architecture imposed by the synthesis, for instance Pd present in Zn-poor regions.

The slightly contracted lattice parameters observed for the FCC Pd phase implies that there was some incorporation of Zn into the Pd lattice to form a α-PdZn alloy. At 375 °C and above, both the α-PdZn and β_1-PdZn phases showed increased amounts of Zn in their

respective structures, consistent with an increased amount of zero valent Zn. The α-PdZn and β_1-PdZn phases co-existed at all reduction temperatures investigated here, suggesting that the α-PdZn phase formed in regions where there was less reducible Zn available. This could either be due to Pd particles being present on regions of the support with low Zn concentrations or it could reflect a gradient in Zn concentration from high to low on going from the outside to the inside of the particles. Previously, the ZnO facet on which the β_1-PdZn alloy grows has even been shown to affect the ease with which it forms[61]. The fact that the size of the α-PdZn domains increased with temperature, seemingly due to sintering, implies that at least some fraction of this phase was present as non-encapsulated particles, since it would be expected that the size of the Pd cores would decrease as the β_1-PdZn phase becomes the dominant structure. Furthermore, the presence of Pd hydride at 40 °C in H_2 after all reduction temperatures indicates that the Pd-rich FCC phase was accessible to the H_2 atmosphere. As observed here and in previous reports, β_1-PdZn does not form a bulk hydride and therefore if the Pd phase was encapsulated by β_1-PdZn it may be expected that it would prevent hydride formation in the Pd core[57].

The role of α-PdZn relative to Pd in dehydrogenation catalysis is not clear although previously, it has been shown to modify CO binding[62] but to behave similarly to Pd metal in the steam reforming of methanol[56]. This Pd-rich phase may be the reason for the lower propylene selectivity compared to the $PdZn/SiO_2$ catalyst previously reported[21].

The XRD results suggest that two different types of alloys formed as ZnO was reduced in the presence of Pd. However, no pure metallic Zn was observed suggesting that this is highly unfavorable under the conditions and therefore it is likely once Zn cations were reduced to zero valent Zn, they were rapidly incorporated into an alloy with Pd. Considering the much lower melting point of Zn relative to Pd, metallic Zn atoms produced from reduction of ZnO are more mobile than Pd atoms and hence once reduced, are able to diffuse and form alloys with Pd. The smaller size of the β_1-PdZn domains after reduction at 450-500 °C, relative to the remaining Pd-rich FCC phase suggests that the

incorporation of Zn into Pd particles to form alloys could cause fracture leading to smaller coherently diffracting domains.

The increase in selectivity of $PdZn/Al_2O_3$ relative to Pd/Al_2O_3 for the dehydrogenation of propane at 550 °C is attributed to separation of the Pd atoms due to the formation of PdZn alloys. A geometric modification to the catalyst such as this was suggested by Childers *et al* to give rise to higher rates for structure-insensitive reactions than structure-sensitive reactions. Although the selectivity for the catalyst reported here is not as high as that reported previously (64 % vs 98 % at comparable conversion)[21], the selectivity to propylene was still significantly higher than for pure Pd at the same conversion, showing that the alloys that form do enhance the selectivity. Nonetheless, the lower selectivity does suggest some differences exist in the catalyst structure. The linear to bridge bound CO ratio measured for this catalyst was 1.4 after reduction at 500 °C while the catalyst reported by Childers *et al* had a value of 2.5, indicating more efficient isolation of the Pd atoms. This difference in ratio for the $PdZn/Al_2O_3$ catalyst may be due to the contribution to bridge bound CO from the Pd-rich, α-PdZn alloy. Furthermore since the β_1-PdZn phase was Pd-rich, this also likely contributes to bridge bound CO.

Since XRD is a bulk technique it is not possible to conclusively determine that the surface of the catalyst presents the β_1-PdZn phase under reaction conditions. Additionally, although the propane dehydrogenation reaction provides a reducing environment, it is possible that changes to the surface including reconstruction could be possible under real reaction conditions. Nevertheless, the observation of this phase at low temperatures, during the first stages of alloy formation does suggest that it is present at the surface of the nanoparticles. This is supported by the DRIFTS of adsorbed CO which provides strong evidence that the surface presents a significant fraction of isolated Pd sites. Thus it is likely that the enhanced propylene selectivity is due to the formation of the intermetallic β_1-PdZn structure. Additionally, it is evident that the phase assemblage as a function of reduction temperature is somewhat complex and to be fully understood it requires implementation of multiple techniques and the consideration of non-stoichiometric compounds which likely have an impact on catalytic performance.

Conclusions

A $PdZn/Al_2O_3$ catalyst selective for dehydrogenation of propane at 550 °C has been characterized using DRIFTS of adsorbed CO, *in situ* synchrotron XRD and EXAFS to follow its structural evolution during reduction. The combination of DRIFTS and XRD indicated that the β_1-PdZn intermetallic alloy structure formed at temperatures as low as 230 °C, likely first at the surface, but did not form extensively throughout the bulk until 500 °C. DRIFTS results suggested there was little change in the surfaces of the nanoparticles above 325 °C indicated by the plateau in the ratio of linear to bridge bound CO. The high quality XRD data allowed Le Bail refinement to be performed from which it was determined that the intermetallic alloy forming was Pd-rich at all temperatures, but became less Pd-rich with increasing reduction temperature as more Zn incorporated into the structure. In addition to the β_1-PdZn alloy, a solid solution phase with face-center cubic structure (α-PdZn) was present in the catalyst, also becoming more Zn-rich with increasing reduction temperature. These results are consistent with the proposal of Childers *et al* that the catalytically active Pd atoms in the Pd-Zn catalysts are responsible for the high olefin selectivity for propane dehydrogenation.

Acknowledgments

This material is based upon work supported as part of the Institute for Atom-efficient Chemical Transformations (IACT), an Energy Frontier Research Center funded by the U.S. Department of Energy, Office of Science, Office of Basic Energy Sciences. DJC and RJM thank the National Science Foundation (CBET-747646) for financial support. Use of the Advanced Photon Source was supported by the U.S. Department of Energy, Office of Basic Energy Sciences, under contract No. DE-AC02-06CH11357. MRCAT operations are supported by the Department of Energy and the MRCAT member institutions. The authors also acknowledge the use of beamline 11-ID-C.

References

1. R. Ferrando, J. Jellinek and R. L. Johnston, *Chem. Rev.*, 2008, **108**, 845-910.
2. N. Schweitzer, H. L. Xin, E. Nikolla, J. T. Miller and S. Linic, *Top. Catal.*, 2010, **53**, 348-356.
3. E. Casado-Rivera, D. J. Volpe, L. Alden, C. Lind, C. Downie, T. Vazquez-Alvarez, A. C. D. Angelo, F. J. DiSalvo and H. D. Abruna, *J. Am. Chem. Soc.*, 2004, **126**, 4043-4049.
4. H. B. Zhao and B. E. Koel, *J. Catal.*, 2005, **234**, 24-32.
5. J. C. Bauer, X. Chen, Q. S. Liu, T. H. Phan and R. E. Schaak, *J. Mater. Chem.*, 2008, **18**, 275-282.
6. J. Haubrich, D. Loffreda, F. Delbecq, P. Sautet, A. Krupski, C. Becker and K. Wandeltt, *J. Phys. Chem. C*, 2009, **113**, 13947-13967.
7. M. Armbruster, K. Kovnir, M. Behrens, D. Teschner, Y. Grin and R. Schlogl, *J. Am. Chem. Soc.*, 2010, **132**, 14745-14747.
8. X. L. Ji, K. T. Lee, R. Holden, L. Zhang, J. J. Zhang, G. A. Botton, M. Couillard and L. F. Nazar, *Nat. Chem.*, 2010, **2**, 286-293.
9. C. Weilach, S. M. Kozlov, H. H. Holzapfel, K. Fottinger, K. M. Neyman and G. Rupprechter, *J. Phys. Chem. C*, 2012, **116**, 18768-18778.
10. M. Armbruster, R. Schlogl and Y. Grin, *Sci. Technol. Adv. Mater.*, 2014, **15**.
11. G. Sauthoff, *Intermetallics*, Wiley, 2008.
12. N. Iwasa, S. Masuda, N. Ogawa and N. Takezawa, *Appl. Catal. A-Gen.*, 1995, **125**, 145-157.
13. N. Iwasa, T. Mayanagi, W. Nomura, M. Arai and N. Takezawa, *Appl. Catal. A-Gen.*, 2003, **248**, 153-160.
14. C. Rameshan, W. Stadlmayr, C. Weilach, S. Penner, H. Lorenz, M. Havecker, R. Blume, T. Rocha, D. Teschner, A. Knop-Gericke, R. Schlogl, N. Memmel, D. Zemlyanov, G. Rupprechter and B. Klotzer, *Angew. Chem.-Int. Edit.*, 2010, **49**, 3224-3227.
15. A. Ota, E. L. Kunkes, I. Kasatkin, E. Groppo, D. Ferri, B. Poceiro, R. M. N. Yerga and M. Behrens, *J. Catal.*, 2012, **293**, 27-38.
16. M. Armbruster, M. Behrens, K. Fottinger, M. Friedrich, E. Gaudry, S. K. Matam and H. R. Sharma, *Catal. Rev.-Sci. Eng.*, 2013, **55**, 289-367.
17. H. Lorenz, C. Rameshan, T. Bielz, N. Memmel, W. Stadlmayr, L. Mayr, Q. Zhao, S. Soisuwan, B. Klotzer and S. Penner, *ChemCatChem*, 2013, **5**, 1273-1285.
18. M. Nilsson, K. Jansson, P. Jozsa and L. J. Pettersson, *Appl. Catal. B-Environ.*, 2009, **86**, 18-26.
19. L. Bollmann, J. L. Ratts, A. M. Joshi, W. D. Williams, J. Pazmino, Y. V. Joshi, J. T. Miller, A. J. Kropf, W. N. Delgass and F. H. Ribeiro, *J. Catal.*, 2008, **257**, 43-54.
20. A. Sarkany, Z. Zsoldos, B. Furlong, J. W. Hightower and L. Guczi, *J. Catal.*, 1993, **141**, 566-582.
21. D. J. Childers, N. M. Schweitzer, S. M. K. Shahari, R. M. Rioux, J. T. Miller and R. J. Meyer, *J. Catal.*, 2014, **318**, 75-84.
22. E. J. Peterson, B. Halevi, B. Kiefer, M. N. Spilde, A. K. Datye, J. Peterson, L. Daemen, A. Llobet and H. Nakotte, *J. Alloy. Compd.*, 2011, **509**, 1463-1470.

23. C. F. Macrae, I. J. Bruno, J. A. Chisholm, P. R. Edgington, P. McCabe, E. Pidcock, L. Rodriguez-Monge, R. Taylor, J. van de Streek and P. A. Wood, *J. Appl. Crystallogr.*, 2008, **41**, 466-470.
24. H. Okamoto, *Binary Alloy Phase Diagrams* 2edn., American Society for Metals, Metals Park, OH, 1990.
25. Y. H. Chin, R. Dagle, J. L. Hu, A. C. Dohnalkova and Y. Wang, *Catal. Today*, 2002, **77**, 79-88.
26. A. Karim, T. Conant and A. Datye, *J. Catal.*, 2006, **243**, 420-427.
27. T. Conant, A. M. Karim, V. Lebarbier, Y. Wang, F. Girgsdies, R. Schlogl and A. Datye, *J. Catal.*, 2008, **257**, 64-70.
28. M. W. Tew, H. Emerich and J. A. van Bokhoven, *J. Phys. Chem. C*, 2011, **115**, 8457-8465.
29. S. D. M. Jacques, O. Leynaud, D. Strusevich, A. M. Beale, G. Sankar, C. M. Martin and P. Barnes, *Angew. Chem.-Int. Edit.*, 2006, **45**, 445-448.
30. S. D. M. Jacques, O. Leynaud, D. Strusevich, P. Stukas, P. Barnes, G. Sankar, M. Sheehy, M. G. O'Brien, A. Iglesias-Juez and A. M. Beale, *Catal. Today*, 2009, **145**, 204-212.
31. M. G. O'Brien, A. M. Beale, S. D. M. Jacques, M. Di Michiel and B. M. Weckhuysen, *Appl. Catal. A-Gen.*, 2011, **391**, 468-476.
32. M. A. Newton, M. Di Michiel, A. Kubacka, A. Iglesias-Juez and M. Fernandez-Garcia, *Angew. Chem.-Int. Edit.*, 2012, **51**, 2363-2367.
33. D. Ferri, M. A. Newton, M. Di Michiel, G. L. Chiarello, S. Yoon, Y. Lu and J. Andrieux, *Angew. Chem.-Int. Edit.*, 2014, **53**, 8890-8894.
34. J. R. Gallagher, T. Li, H. Y. Zhao, J. J. Liu, Y. Lei, X. Y. Zhang, Y. Ren, J. W. Elam, R. J. Meyer, R. E. Winans and J. T. Miller, *Catal. Sci. Technol.*, 2014, **4**, 3053-3063.
35. M. A. Newton, M. Di Michiel, D. Ferri, M. Fernandez-Garcia, A. M. Beale, S. D. M. Jacques, P. J. Chupas and K. W. Chapman, *Catal. Surv. Asia*, 2014, **18**, 134-148.
36. T. Ressler, *J. Synchrot. Radiat.*, 1998, **5**, 118-122.
37. J. J. Rehr, J. M. Deleon, S. I. Zabinsky and R. C. Albers, *J. Am. Chem. Soc.*, 1991, **113**, 5135-5140.
38. D. C. Bazin, D. A. Sayers and J. J. Rehr, *J. Phys. Chem. B*, 1997, **101**, 11040-11050.
39. G. Agostini, A. Piovano, L. Bertinetti, R. Pellegrini, G. Leofanti, E. Groppo and C. Lamberti, *J. Phys. Chem. C*, 2014, **118**, 4085-4094.
40. P. J. Chupas, K. W. Chapman, C. Kurtz, J. C. Hanson, P. L. Lee and C. P. Grey, *J. Appl. Crystallogr.*, 2008, **41**, 822-824.
41. P. J. Chupas, M. F. Ciraolo, J. C. Hanson and C. P. Grey, *J. Am. Chem. Soc.*, 2001, **123**, 1694-1702.
42. A. P. Hammersley, S. O. Svensson, M. Hanfland, A. N. Fitch and D. Hausermann, *High Pressure Res.*, 1996, **14**, 235-248.
43. A. Le Bail, H. Duroy and J. L. Fourquet, *Mater. Res. Bull.*, 1988, **23**, 447-452.
44. L. Lutterotti, D. Chateigner, S. Ferrari and J. Ricote, *Thin Solid Films*, 2004, **450**, 34-41.

45. R. Delhez, T. H. Dekeijser and E. J. Mittemeijer, *Fresenius Zeitschrift Fur Analytische Chemie*, 1982, **312**, 1-16.
46. L. Lutterotti and P. Scardi, *J. Appl. Crystallogr.*, 1990, **23**, 246-252.
47. M. A. Vannice and C. C. Twu, *J. Chem. Phys.*, 1981, **75**, 5944-5948.
48. J. Barbier, *Applied Catalysis*, 1986, **23**, 225-243.
49. J. A. Moulijn, A. E. van Diepen and F. Kapteijn, *Appl. Catal. A-Gen.*, 2001, **212**, 3-16.
50. J. E. Penner-Hahn, in *eLS*, John Wiley & Sons, Ltd, 2001.
51. T. Lear, R. Marshall, J. A. Lopez-Sanchez, S. D. Jackson, T. M. Klapotke, M. Baumer, G. Rupprechter, H. J. Freund and D. Lennon, *J. Chem. Phys.*, 2005, **123**.
52. J. L. Lu, B. S. Fu, M. C. Kung, G. M. Xiao, J. W. Elam, H. H. Kung and P. C. Stair, *Science*, 2012, **335**, 1205-1208.
53. V. Lebarbier, R. Dagle, T. Conant, J. M. Vohs, A. K. Datye and Y. Wang, *Catal. Lett.*, 2008, **122**, 223-227.
54. R. W. G. Wyckoff, *Second edition. Interscience Publishers, New York, New York*, Interscience Publishers, New York, 1963.
55. M. Friedrich, D. Teschner, A. Knop-Gericke and M. Armbruster, *J. Catal.*, 2012, **285**, 41-47.
56. B. Halevi, E. J. Peterson, A. Roy, A. DeLariva, E. Jeroro, F. Gao, Y. Wang, J. M. Vohs, B. Kiefer, E. Kunkes, M. Havecker, M. Behrens, R. Schlogl and A. K. Datye, *J. Catal.*, 2012, **291**, 44-54.
57. S. Penner, B. Jenewein, H. Gabasch, B. Klotzer, D. Wang, A. Knop-Gericke, R. Schlogl and K. Hayek, *J. Catal.*, 2006, **241**, 14-19.
58. Y. Uemura, Y. Inada, Y. Niwa, M. Kimura, K. K. Bando, A. Yagishita, Y. Iwasawa and M. Nomura, *Phys. Chem. Chem. Phys.*, 2012, **14**, 2152-2158.
59. K. Fottinger, J. A. van Bokhoven, M. Nachtegaal and G. Rupprechter, *J. Phys. Chem. Lett.*, 2011, **2**, 428-433.
60. S. Kou and Y. A. Chang, *Acta Metallurgica*, 1975, **23**, 1185-1190.
61. H. Zhang, J. M. Sun, V. L. Dagle, B. Halevi, A. K. Datye and Y. Wang, *ACS Catalysis*, 2014, **4**, 2379-2386.
62. R. S. Johnson, A. DeLaRiva, V. Ashbacher, B. Halevi, C. J. Villanueva, G. K. Smith, S. Lin, A. K. Datye and H. Guo, *Phys. Chem. Chem. Phys.*, 2013, **15**, 7768-7776.